A printed Yagi–Uda antenna for application in magnetic resonance thermometry guided microwave hyperthermia applicators

Document status and date:
Published: 08/02/2017

Document Version:
Publisher's PDF, also known as Version of Record (includes final page, issue and volume numbers)

Please check the document version of this publication:

• A submitted manuscript is the version of the article upon submission and before peer-review. There can be important differences between the submitted version and the official published version of record. People interested in the research are advised to contact the author for the final version of the publication, or visit the DOI to the publisher's website.
• The final author version and the galley proof are versions of the publication after peer review.
• The final published version features the final layout of the paper including the volume, issue and page numbers.
[Link to publication](#)

A printed Yagi–Uda antenna for application in magnetic resonance thermometry guided microwave hyperthermia applicators

You may also be interested in:

A printed Yagi–Uda antenna for application in magnetic resonance thermometry guided microwave hyperthermia applicators

M M Paulides[1], R M C Mestrom[2], G Salim[3], B B Adela[2], W C M Numan[1], T Drizdal[1], D T B Yeo[4] and A B Smolders[2]

[1] Department of Radiation Oncology, Erasmus University Medical Center, Cancer Institute, Rotterdam, Netherlands
[2] Department of Electrical Engineering, Eindhoven University of Technology, Eindhoven, Netherlands
[3] Department of Radiology and Nuclear Imaging, Erasmus University Medical Center, Rotterdam, Netherlands
[4] General Electric Global Research, Niskayuna, NY, United States of America

E-mail: m.paulides@erasmusmc.nl

CrossMark

Abstract

Biological studies and clinical trials show that addition of hyperthermia stimulates conventional cancer treatment modalities and significantly improves treatment outcome. This supra-additive stimulation can be optimized by adaptive hyperthermia to counteract strong and dynamic thermoregulation. The only clinically proven method for the 3D non-invasive temperature monitoring required is by magnetic resonance (MR) temperature imaging, but the currently available set of MR compatible hyperthermia applicators lack the degree of heat control required. In this work, we present the design and validation of a high-frequency (433 MHz ISM band) printed circuit board antenna with a very low MR-footprint. This design is ideally suited for use in a range of hyperthermia applicator configurations. Experiments emulating the clinical situation show excellent matching properties of the antenna over a 7.2% bandwidth ($S_{11} < -15$ dB). Its strongly directional radiation properties minimize inter-element coupling for typical array configurations ($S_{21} < -23$ dB). MR imaging distortion by the antenna was found negligible and MR temperature imaging in a homogeneous muscle phantom was highly correlated with gold-standard probe measurements (root mean square error: RMSE = 0.51 °C

and $R^2 = 0.99$). This work paves the way for tailored MR imaging guided hyperthermia devices ranging from single antenna or incoherent antenna-arrays, to real-time adaptive hyperthermia with phased-arrays.

(Some figures may appear in colour only in the online journal)

Introduction

Extensive biologic research has shown that hyperthermia is one of the most potent modifiers of radiation known today (Overgaard 2013) and that it can also be used to selectively enhance the effects of several chemotherapies (van der Zee 2002, Kampinga 2006). During hyperthermia treatments, tissue is heated to 39–44 °C for 60–90 min (Datta *et al* 2015). Added to radiotherapy and/or chemotherapy, the impact of hyperthermia on the local control (Datta *et al* 2015) and even survival (Issels 2010, Issels 2015, Paulides *et al* 2016) was demonstrated through many clinical trials in various tumor sites. Importantly, in these studies, no increase in late toxicity by hyperthermia was found. Hyperthermia in these trials was generally induced by using external electromagnetic incoherent (for superficial tumors) or phased-array (for tumors extending to deeper than 4 cm from the skin) applicators containing up to 12 independently controlled channels, i.e. antennas or antenna pairs. The location, shape and size of the heating pattern is controlled by setting the amplitude and phase of the individual radiofrequency (RF) signals (Fenn *et al* 1996, Nadobny *et al* 2002, Franckena *et al* 2010). Although existing deep RF hyperthermia devices, particularly those operating at 60–100 MHz, have demonstrated their suitability in positive clinical trials, high temperatures induced in normal tissues still restrict achieving the optimum temperature range in the tumor (van Rhoon 2016). Analysis of clinical results showed that achieving higher temperatures would indeed convert to improved clinical outcomes (Jones *et al* 2006, Franckena *et al* 2009, van Rhoon 2016).

Since the focus diameter generated with a cylindrical phased array is minimum one-third of the wavelength in tissue (Paulides *et al* 2005b), 'microwave' frequencies (>300 MHz) would allow for more selective heating. Simulation studies showed that a combination of increasing the number of independent channels (Henke *et al* 2001), smart array design (Togni *et al* 2013) and advanced treatment planning (Paulides *et al* 2013) can effectively counteract the reduced penetration depth at these frequencies. We demonstrated this concept by our HYPERcollar3D (figure 1), which can heat deeply located tumors in the entire head and neck region (Rijnen *et al* 2015, Paulides *et al* 2016). Selective heating requires more advanced monitoring to precisely heat the desired region and to prevent unwanted over-heating in normal tissues. In the clinic, temperatures are generally measured by temperature probes, which can cause morbidity and provide a very poor spatial sampling of the temperature distribution (van der Zee *et al* 1998, Wust *et al* 2006). Magnetic resonance (MR) temperature imaging (MRTI), provides a more complete 3D temperature image without the risk of toxicity (van Rhoon and Wust 2005). Since MRTI is very demanding in terms of field homogeneity and signal-to-noise (SNR) ratio, high constraints exist for the MR compatibility of the antennas. Also vice versa, MRTI should not induce parasitic currents in the antennas, thereby confounding RF heating performance and affecting the MR scanner's RF transmit field ($B1+$) and gradient performance. In this study, we investigated a novel antenna design that is low-cost, reproducible, and inherently MR compatible.
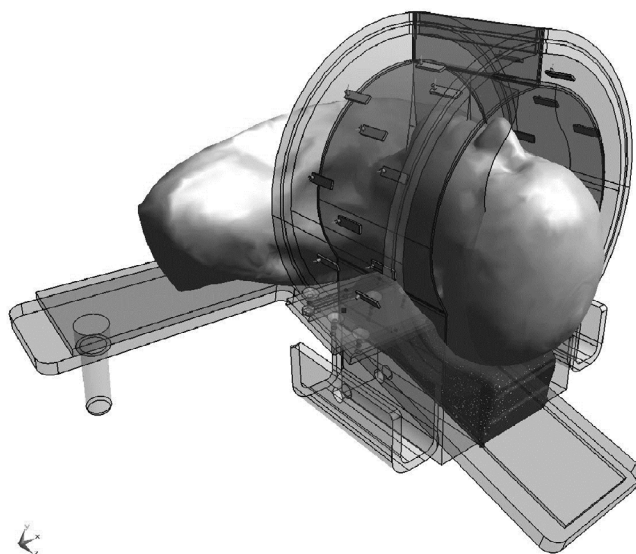
Figure 1. 3D Model of the Hypercollar 3D applicator (Rijnen *et al* 2015), showing three rings of patch antennas in a waterbolus, surrounding a patient. Each antenna can be phase and amplitude controlled, such that their combined output creates an electromagnetic interference pattern that heats a target area.

Although many techniques for non-invasive thermometry (NIT) during RF hyperthermia exist, only MRTI has shown sufficiently accurate to enter the clinic (Gellermann *et al* 2005, van Rhoon and Wust 2005). Clinical MR-RF hyperthermia devices have been developed for the pelvic region (100 MHz) (Gellermann *et al* 2005) and extremity tumors (140 MHz) (Cheng *et al* 2007, Stakhursky *et al* 2009). Recently, also heating using the imaging coils was demonstrated in a (Yeo *et al* 2011, Winter *et al* 2013, 2015), but this approach restricts the operation frequency choice to the Larmor frequency (64 or 128 MHz). All previous approaches use RF waves ($<$300 MHz) for heating, leading to poor heat focusing and focus-shaping possibilities. For the head and neck region, we experimentally showed the feasibility of MR guided hyperthermia using a microwave frequency, i.e. 433.92 MHz. Hereto, we have developed an MR compatible laboratory prototype of the HYPERcollar and demonstrated MRTI accuracy in a neck-mimicking phantom (Paulides *et al* 2014). Still, although MRTI during heating is feasible, accurate measurements require that image distortions by the applicator are reduced to the absolute minimum (Gellermann *et al* 2005, Gellermann *et al* 2008). In this work, we focus on creating a novel antenna as building block for applicators with maximum MR transparency aimed at MR measurements with the highest signal-to-noise-ratio (SNR) possible.

The MR thermometry technique used in this paper and generally in hyperthermia, is the proton resonance frequency shift (PRFS) method (Rieke and Butts Pauly 2008). Accurate MRTI *in vivo* however is challenge due to the tissue transitions, air cavities and prominence of motion (respiration, cardiac), as well as magnetic field (B_0) distortions by the drift of the scanner, temperature changes, and the presence of a hyperthermia applicator (Rieke and Butts Pauly 2008, Ludemann *et al* 2010, Winter *et al* 2016). In this work, we used a new PRFS-based method, i.e. 2MT-PRFS (Salim *et al* 2015), which corrects for $T2^*$ effects, water-fat ratio, and phase at TE $= 0$ using off-resonance estimation, and applies fat-correction (Hofstetter *et al* 2011). Experiments in a phantom showed that this technique outperforms a conventional PRFS method (Salim *et al* 2015).

In this paper, we present the design and experimental validation of a printed circuit board (PCB) Yagi–Uda antenna, to be used in MR compatible hyperthermia applicators operating in the 433 MHz ISM band[5]. We specify the requirements, discuss our design approach and present the antenna design. A coherent set of measurements and simulations was conducted to investigate the performance of the antenna in hyperthermia applications and analyze the potential for MR guided single-antenna and multi-antenna phased-array applicators. If the antenna fulfills all requirements, it will bring improvements in antenna durability and reproducibility, at reduced production cost, compared to current antenna designs used in hyperthermia.

Materials and methods

Requirements and design process

An overview of the design requirements based on clinical experience from existing applicators (Paulides *et al* 2007b, Rijnen *et al* 2015) and the validated MR compatible prototype (Paulides *et al* 2014, Tarasek 2014), is given in table 1. Although most requirements concern single antenna metrics, these have been formulated such that successful operation of the antenna in array configurations is guaranteed.

Earlier, we found that target-selective heating requires the use of microwave frequencies, such as 433.92 MHz (Paulides *et al* 2005a), resulting in a full-width-half-maximum of the ellipsoidal heating region's short axis of 3.5 cm. Further, achieving the required thermal distribution in the tumor requires the antenna elements to handle up to 150 W per antenna (Bakker *et al* 2010, Rijnen *et al* 2013). The antenna should be able to handle a varying environment because, to increase energy coupling from the antenna to the patient, the antenna is placed inside a 'water bolus' (van der Zee 2002) bag filled with de-ionized (DI) water (figure 1) of varying temperature and thickness. This water is controlled at a low temperature (25 °C $\pm$ 2 °C) to simultaneously cool the patient's skin and stabilize antenna performance. In Paulides *et al* (2007a), we found that a 5% frequency bandwidth provides sufficient robustness against variations in the water environment. To avoid excessive heating of subcutaneous tissue and to reduce high power absorption at fat-muscle transitions, the tangential component(s) of the electric field inside the patient should be much larger than components normal to the patient (Paulides *et al* 2007a). A dominant tangential electric field also results in optimal constructive interference of the electromagnetic waves (Paulides *et al* 2007a). To reduce power losses in the water bolus, the antennas should be positioned at an optimal distance from the patient skin. This optimal distance is as close as possible to the patient, but far enough to avoid excessive influence of the patient on the radiation characteristics (so-called loading) of the antennas. Typically, a distance of half a wavelength in water ($h = 4$ cm at 433.92 MHz) is used (Paulides *et al* 2007a). To avoid additional matching circuits between the power amplifier and antenna, a pre-matched antenna design is desired. To reduce performance deterioration in an array arrangement, the mutual coupling between the antenna elements should be low, preferably less than -20 dB (Wust *et al* 2001). Note that this requirement can be separated into the need for a directive antenna and the impact of its location and orientation in the antenna array. In this paper, we focus on directivity to enable using the antenna in a range of array configurations, like planar and circular arrays.

MR compatibility of any device entails the minimization of the device's interaction with the scanner's main static magnetic field, switching gradient fields, transmit RF fields, and the use of materials that may yield spurious proton signals. Static field interaction and spurious proton

---

[5] ISM band: frequency range allocated for Industry, Science and Medicine.

Table 1. The requirements and aims for the antenna design.

Parameter	Requirement/aim
Operating frequency	433.92 MHz
Frequency bandwidth (relative)	>5% (>21.7 MHz)
Power-handling level	150 W
Input reflection coefficient	$\leqslant -15$ dB
Radiation medium	De-ionized water
Antenna interface	Coaxial cable
Ratio of the tangential component versus the total electric field	>0.8 at the skin surface for the antenna aperture
Operating temperature	25 ± 2 °C
Mutual coupling	$\leqslant -20$ dB
Main magnetic field distortion	$\leqslant 1$ ppm field distortion[a]
Gradient field distortion	No conducting loops[a]
MR RF distortion	Small cross-section in the $B1+$ and $B1-$ directions, absence of resonating structures at 64 MHz[a]

[a] These requirements can also be met by accurate MRTI measurements in a relevant region-of-interest (ROI).

signal can be generally avoided by material choices, i.e. by avoiding ferromagnetic materials to minimize any adverse effect on the static magnetic field ($B0$). Gradient switching-induced eddy currents may heat the device and dampen the gradient field changes that can be applied. Their occurrence can be reduced by limiting the size of current paths, generally aiming for small continuous conducting surfaces, by avoiding conductive loop structures, and/or the use of thin conductive materials. The continuous shared copper ground plane of the HYPERcollar3D antenna array (Rijnen *et al* 2015) would for example shield the patient from MR imaging. In earlier work, we showed that a reduced size and optimized orientation of the conductive elements of a coaxial-fed patch antenna effectively improved MR measurement performance (Paulides *et al* 2014). However, further reductions would potentially allow faster MR sequences that use fast switching gradients, e.g. echo-planar-imaging. The RF properties of the device should also be aimed towards presenting a high impedance to transmit or receive coils in the MR frequency band. In previous work, we showed that the base layout of a hyperthermia device already provides a suitable orientation and position (Paulides *et al* 2014). In addition, even without reducing common mode interference by cable-traps, no distortion of the $B1 +$ RF field at the Larmor frequency (64 MHz at 1.5 T) was observed (Paulides *et al* 2014).

Although the system operates at a fixed frequency of 433.92 MHz, a minimum antenna bandwidth of 5% (21.7 MHz) is required as a surrogate for robustness against variations in material properties, production tolerances, and varying environmental conditions such as a changing water temperature.

Antenna design and optimization using electromagnetic modelling

In this study, we adapted and analyzed the well-known Yagi–Uda antenna concept for our application (Balanis 2005). This antenna consists of a dipole antenna that is made more directional using two passive elements: a reflector (backside) and a director (frontside). Earlier, we demonstrated the feasibility of this concept (Adela *et al* 2013). Figure 2 shows the geometry optimized for operation at 433.92 MHz. The optimal design was found by manual tuning after an initial theoretical estimate for the antenna, its director and reflector (Balanis 2005).

All simulations used to optimize the design were done with the Finite Integration Technique solver in CST Microwave Studio (CST AG, Darmstadt, Germany). The metal parts of the antenna were modeled as perfect electric conductors (PEC). Air was modelled using vacuum properties. The PCB-board material (FR4 by Eurocircuits) was modeled with a relative permittivity of $\varepsilon_r = 4.3$ and loss tangent of $\tan\delta = 0.025$. DI water properties were taken at $T = 25$ °C: $\varepsilon_r = 77$, and $\sigma = 0.04$ S m^{-1} (DI water is still somewhat lossy at 433.92 MHz). Absorbing boundary conditions (absorption $\geqslant 99.9\%$) were used at the sides of the simulation domain to avoid reflections. Figure 2 also shows the 'clinical environment' for which the antenna is optimized. As described earlier, the antenna is embedded in a waterbolus, filled with DI water that is used for an efficient transfer of electromagnetic energy into the patient and for cooling the skin and the antennas. The waterbolus was modelled by an 82 mm thick water volume of de-ionized water, with absorbing boundaries at the four remaining sides to model an infinite water slab. Note that DI water at 433.92 MHz is still somewhat lossy (0.04 S m^{-1}). As in Paulides, Bakker, Chavannes and Van Rhoon (Paulides *et al* 2007a), the patient was modelled by a muscle region with its interface at 40 mm from the antenna. Taking these environmental parameters into account, the dimensions of the antenna (in water: figure 2) and the feedlines (crossing the water–air interface: figure 2), were tuned to match to the required input impedance at the connector in air of 50 Ω.

### *Impedance and radiation characteristics*

For low-power characterization, we used the experimental setup of figure 4, which resembles the configuration for the simulations in figure 2 (top). It consists of a Styrofoam container, with inner dimensions of 17.5 cm (x-direction) and 20 cm (y-direction), in which the antenna is partly submerged into the DI water from the bottom of the setup. A floating muscle phantom was prepared following a recipe of Ito, Furuya, Okano and Hamada (Ito *et al* 2001). To study the robustness of the antenna input reflection coefficient to varying conditions in the clinic, we varied the phantom-antenna distance (d) between 20 mm, 40 mm and 80 mm and the temperature of the de-ionized water ($T_{DI_{water}}$) in steps of 5 °C in the range of 20–35 °C, like in Paulides, Bakker, Neufeld, van der Zee, Jansen, Levendag and van Rhoon (Paulides *et al* 2007b). The ratio between the tangential (E_y) and total electric field for this antenna design was quantified using post-processing of the simulation results in Matlab (Mathworks, Natick MA, USA).

Cross-coupling in array configurations

In antenna array configurations, the mutual coupling between antennas is specifically of interest. Strong coupling affects the impedance matching of the antennas and can affect the heating and heating steering possibilities of the applicator. The configuration for measuring the mutual coupling in an array set-up is shown in figure 7. Because the patient acts as a very effective RF load in hyperthermia applicators at higher frequencies, we only analyzed directly adjacent antennas since these exhibit the strongest interactions. The experimental set-up was similar to the single element arrangement (figure 4), but was modified to allow placement of two antennas in four different arrangements. Distances (figure 7) were chosen to match those of a clinically used applicator (Paulides *et al* 2007b):

- $d_1 =$ broadside parallel array distance, 40 mm or 80 mm;
- $d_2 =$ staggered parallel distance, 20 mm or 60 mm.
- $a = 15$ mm for the staggered case
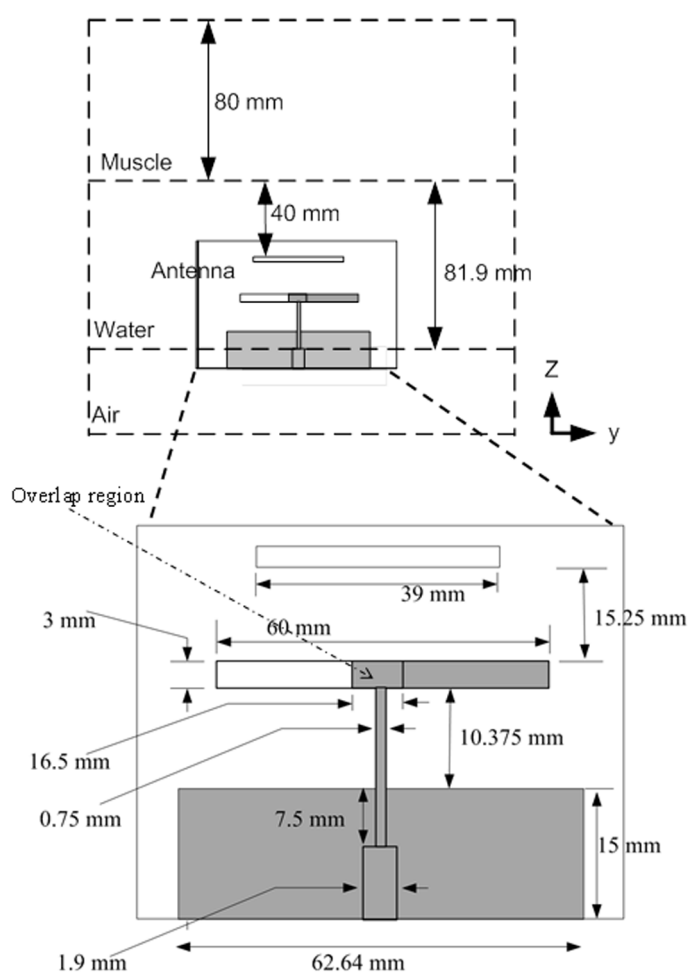
Figure 2. Schematic drawings of the setup (nominal situation: $h = 40\,mm$) used for optimization of the printed antenna mimicking the clinical environment (top) and the final printed antenna design and its optimized dimensions (bottom).

High power handling

During hyperthermia treatments, the antennas have to withstand high input powers up to 150 W. To validate the power handling capability of the antenna, we used the single element arrangement (figure 4). An RF power amplifier, operating at 433.92 MHz was attached, which is capable of generating a maximum power of 150 W (Medlogix, Medical Solutions, Italy). To monitor the power generated by the power amplifier, we used a digital power meter (EMP-442A, Agilent, USA) connected to the antenna through a -27 dB directional coupler (3020A, Narda, USA) and a 6 dB attenuator (R412720000, Radial, USA). This setup was also used to measure the reflected power from the antenna. In total, the power measured by the power meter was 33 dB less than the input power to the antenna. Starting from an input power of 0 W and incrementing the power by 10 W every 5 min, we recorded the input reflection coefficient, the temperature of the water and the temperature at the SMA connector. Once the power reached 180 W, we stepwise decreased the power down to 10 W. Note that, in contradiction to clinical operation, the water was not circulated to assess the high-power performance of the antenna under worst-case conditions.

MR compatibility and MRTI accuracy

In these experiments, we analyzed the MR-compatibility of the antenna, its heating profile and the feasibility and accuracy of MRTI. The setup of figure 4 was placed inside a 1.5 T MR scanner (Optima MR450w, GE Healthcare, Waukesha, WI, USA) and the scanner's body-coil was used for transmit and receive of the RF signals. Four closed-tip catheters were inserted into the muscle-equivalent phantom to allow placement of temperature probes during the experiment. In addition, three sunflower oil containers were installed in the setup as fat-references for correcting $B0$ heterogeneities in MRTI post-processing. Prior to the experiments, pre-calibrated Bowman Thermistor probes, supplied by BSD Medical, were inserted into the catheters and used for ground-truth temperature measurements. MRTI was performed using the 2MT-PRFS method, since this method was shown more accurate than conventional corrected PRFS in a similar phantom (Salim *et al* 2015). The 2MT-PRFS requires multi-echo gradient-echo (ME-GRE) images, so we applied ME-GRE scanning with a GE Optima MR450w 1.5 T MRI scanner and the following settings: TR = 300 ms, TE = 3.7, 6.8, 10.2, 13.7, 17.1, 20.6, 24.0 and 27.5 ms, FA = 29°, bandwidth = 50 kHz, matrix = 256 x 256, FOV = 40 × 40 cm, 5 slices, slice thickness = 0.5 cm. To verify MR transparency, we created magnitude images using only one echo (TE = 26.2 ms) of the ME-GRE scan. Before heating, we made a baseline ME-GRE scan. We then applied five cycles of approximately 3 min of heating at 150 W, followed by a period without power during which a ME-GRE scan was acquired. Temperature increase (ΔT) maps were calculated using the 2MT-PRFS method.

The first cycle was also used to assess the SAR pattern of the antenna for various antenna—phantom distances. A short, 3 min, pulse at high power was used to reduce the impact of thermal diffusion on the SAR measurement (Hand *et al* 1989). SAR($t1, t2$) was calculated using $c_v{}^* \Delta T(t1, t2)/\Delta t$, where $\Delta T(t1, t2) \sim \Phi(t_2) - \Phi(t_1)$ (Rieke and Butts Pauly 2008), $\Delta t = t_2 - t_1 = t_{\text{power-off}} - t_{\text{power-on}}$ as extracted from the time-temperature curves of the probes and assuming a c_v of 3630 J/kg/K in the muscle phantom. Note that the actual c_v is unimportant since we will present only normalized SAR distributions in this paper. Further note that $\Phi(t)$ are the phase maps at time t and that the dependency of SAR and ΔT on the spatial coordinates *x*, *y*, *z* are omitted for clarity.

After a total of 23 min for the five heating cycles, the setup was allowed to cool down for another 30 min with regular MRTI measurements. The position of each temperature probe was reconstructed using the catheter tracks measured with a combination of the MR magnitude images and the measured insertion depth. Averaging of the MRTI scans in an in-plane region-of-interest (ROI) of 5 × 5 pixels around each probe was applied to reduce noise in this comparison. The agreement between probes and MRTI was quantified by calculating the root mean squared error (RMSE) and the correlation coefficient (R^2).

Results

The geometry of the printed Yagi–Uda antenna as optimized for operation at 433.92 MHz in the clinic mimicking environment is shown in figure 2. The antenna is small in size (62 mm) and can be easily inserted into the water bolus. In addition, the antenna does not require a ground plane parallel to the RF coil of the MR scanner, enhancing the transparency to the scanner's gradient, but has a ground plane perpendicular to the RF coil of the MR scanner as a reflector in the Yagi–Uda antenna. The base of the antenna contains a microstrip transmission line connected to the coaxial feed point and is surrounded by air or mounting material. The antenna's

top part (the top 41.9 mm) is surrounded by DI water and contains part of the ground-plane/reflector, the dipole and the director. The parallel strip-fed dipole arms are printed on opposite sides of the dielectric substrate (FR4). The size of the overlap region (see figure 2) between the two arms was used as a geometrical parameter to match the antenna impedance. The directing metal strip at the top of the substrate and the ground of the microstrip line both increase the directivity of the antenna. The antenna is fed by a 50 Ω microstrip line that transforms into a twin-lead transmission line. Figure 3 shows the prototype that was manufactured on a 1.6 mm FR4 substrate according to the layout of figure 2. The metallic parts (copper) were laminated by a thin layer of anti-corrosion material.

Impedance and radiation characteristics

The simulated and measured input reflection coefficient of the antenna for the nominal situation ($T_{DI_{water}} = 25$ °C, $h = 40$ mm) are depicted in figure 4. The measured response shows that the antenna is matched at 433.92 MHz, with a -15 dB impedance bandwidth of 31 MHz (7.2%, from 416 to 447 MHz). Excellent agreement between simulation and experiment is observed, i.e. the resonance frequency prediction error is 1 MHz and the value of the reflection at resonance deviates only 4 dB.

Figure 5 depicts the simulated ratio between E_y and the total electric field (E_{tot}) for the *E*-plane of the antenna. The tangential component (E_y) clearly dominates the electric-field at the water-muscle transition. The ratio $|E_y|/|E_{tot}|$ is $> 80\%$ at this transition for y in the range of -5 to 5 cm, which is even wider than the antenna itself and resembles our proven patch antenna design (Paulides *et al* 2007a).
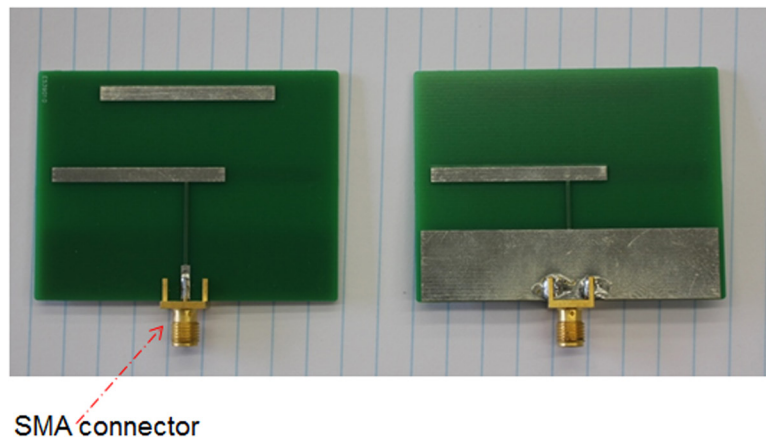
Figure 6(a) shows the measured reflection coefficients for variation in h and $T_{DI_{water}}$. All distances h do not impede antenna operation. At a distance h of 20 mm, the presence of the muscle phantom reduces the -15 dB impedance bandwidth to 4.9% due to loading of the antenna. Figure 6(b) shows that the antenna behavior is quite robust for temperature variations. Only at a high water temperatures (35 °C), the antenna is detuned too much. Hence, especially when the water temperature is controlled to 25 ± 2 °C, the antenna is sufficiently robust against temperature changes of its water embedding.

Cross-coupling in array configurations

Figure 7 shows the measured mutual coupling for broadside ($d_1 = 40$ mm and 80 mm) and staggered parallel ($d_2 = 20$ mm and 60 mm) arrangements. Note that these values are meaningful only within the impedance bandwidth of the antenna: 416–447 MHz. As expected from Paulides, Bakker, Chavannes and Van Rhoon (Paulides *et al* 2007a), the worst coupling at 433 MHz was found for a broadside arrangement (-23 dB) and the lowest coupling in the staggered arrangement (< -30 dB). Temperature variations of 25 ± 2 °C had a negligible influence on the mutual coupling (data not shown). In summary, the antenna met the specification in table 1.

High power handling

Although increases in power also led to an increased temperature of the water embedding and the SMA connector, the worst case reflection coefficient remained below -15 dB at the operating frequency, even without applying water circulation.

Figure 3. The manufactured printed Yagi–Uda antenna, front (left) and back (right).
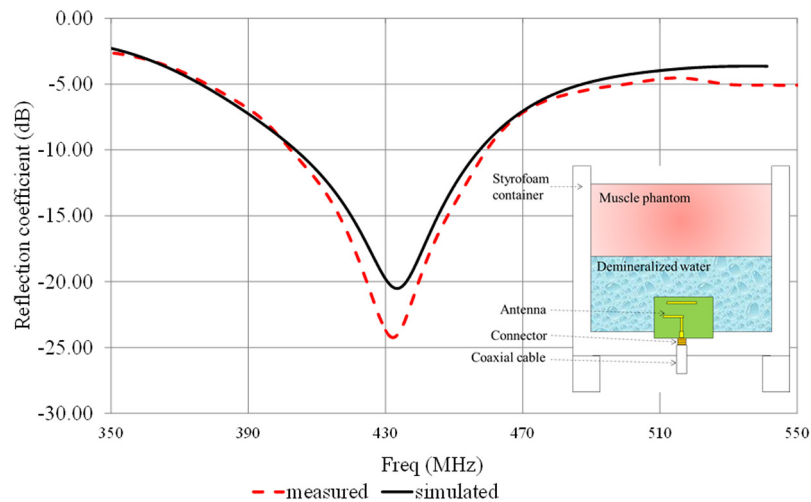
Figure 4. Simulated and measured reflection coefficient for the nominal situation ($T_{DI_{water}} = 25$ °C, $h = 40$ mm) and the experimental setup used in the measurements (inlay).

MR compatibility and MRTI accuracy

Figure 8 shows the magnitude ($t = 1$ min), power absorption, SAR ($t = 1, 6$ min), and temperature increase maps, i.e. ΔT ($t = 1, 24$ min), of the setups with varying antenna phantom distances. In contradiction to common practice in MRTI, the maps are deliberately not spatially averaged to enable a more direct analysis of the measurement results. Note that there was a delay of 2 s between the MR measurements before application of power so Δt was calculated used the heating time deduced from the temperature probe measurements. The magnitude scans show that the impact of the antenna and connector are negligible: apart from a dark line due to the PCB, only a slight dark region at the bottom of the antenna is noticed. Additional MR measurements demonstrated that these dark regions were caused by slightly
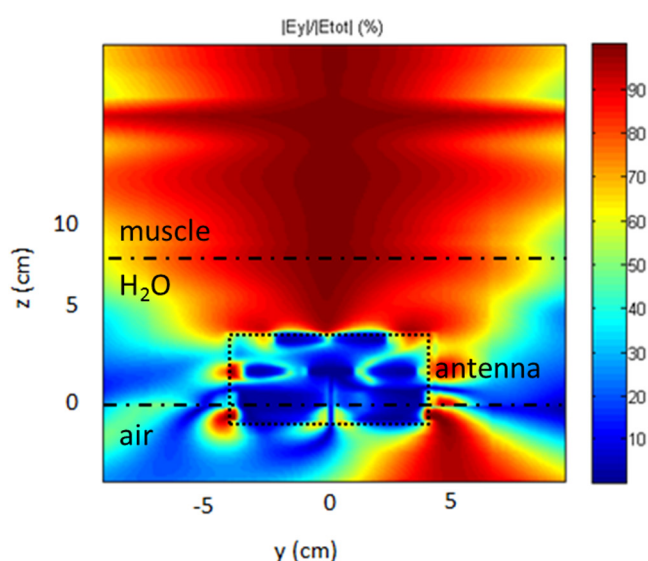
Figure 5. The ratio of tangential (E_y) to the total electric field (E_{tot}) in the *E*-plane of the antenna. The dotted line indicates the outer contour of the antenna and the dash-dot lines represent the transitions from air to DI water (H_2O) and from H_2O to the muscle phantom. This setup closely resembles the experimental setup of figure 4, except that absorbing boundary conditions are applied in *x* and *y*-direction.

ferro-magnetic SMA connectors. In the 2MT-PRFS based ΔT map, all disturbances are substantially reduced. Both magnitude and MRTI results show the excellent MR transparency of the antenna.

The SAR maps of figure 8 demonstrate that the antenna indeed acts as expected. For a close antenna distance ($h = 20\,mm$), the SAR is confined in the *y*-direction, which increases for a 40 mm distance. These SAR distributions, particularly the most realistic cases ($h = 20$ and 40 mm), show the applicability of the antenna for MR guided superficial hyperthermia. Note that the blue probe, which was located 3.5 cm from the water-muscle interface and just within the 25% iso-SAR zone, still measured a local SAR as high as 60 W kg^{-1}, at the 150 W applied power.

Figure 9 visualizes the transient temperature measured in the homogeneous muscle equivalent phantom using temperature probes and MRTI. This figure clearly shows the temperature increase cycles applied and the moments at which MRTI measurements were taken. Note that the measurements of both systems were slightly mismatched in time due to a system clock synchronization issue. This figure demonstrates that the antenna does not impede highly accurate MRTI. The temperatures measured in the MRTI regions of interest (ROIs) closely match the temperature curves measured by the high resistive probes. This agreement can be quantified by the low measurement error (RMSE = 0.51 °C) and the high correlation coefficient ($R^2 = 0.99$).

Discussion

A printed Yagi–Uda antenna was developed since this implementation provides a low-cost, reproducible, more directional and MR transparent alternative to currently existing antenna designs. Analysis against predefined specifications reveals excellent performance for the quantitative
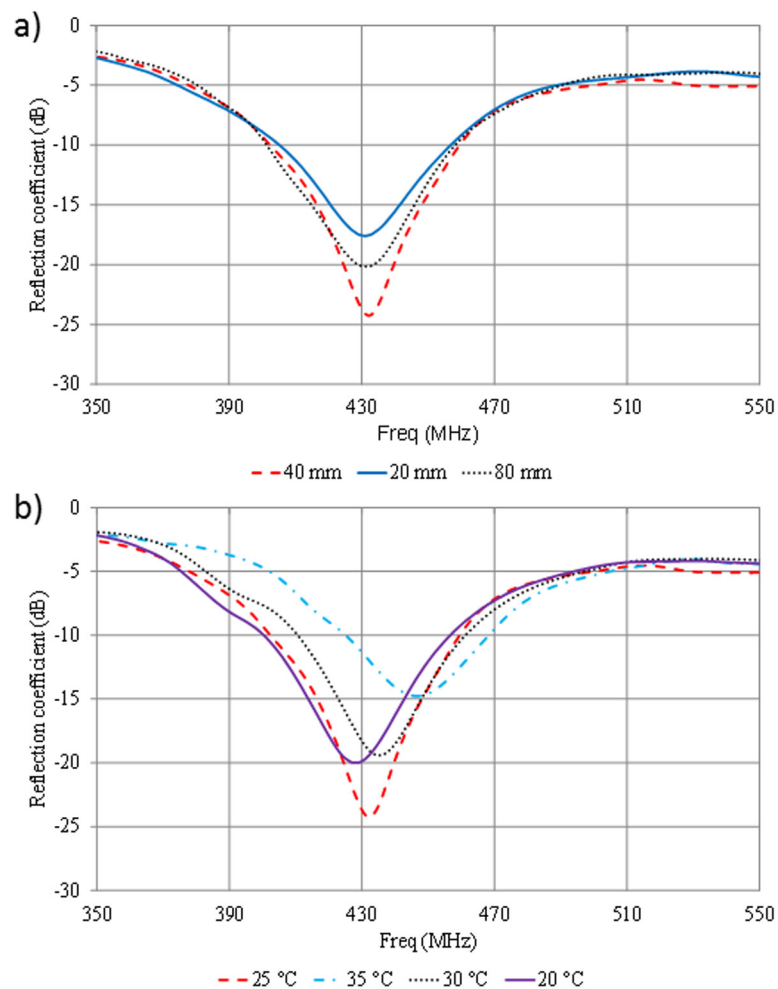
Figure 6. Measured robustness of the reflection coefficient of the antenna against variations in (a) water-muscle phantom distance (*h*) and (b) the temperature of the water embedding ($T_{\mathrm{DI_{water}}}$).

measures. The MR images and highly accurate MRTI results further show the antenna's MR transparency and the feasibility of MR thermometry during application of hyperthermia.

In this paper, only single antenna operation was demonstrated. However, MR guided operation has most potential for phased array applicators since these provide more possibilities to adapt the heating based on MRTI feedback. Earlier, we demonstrated phased array performance using an array of patch antennas that have similar characteristics, except for an inherently worse directivity, poorer reproducibility and higher manufacturing costs (Paulides *et al* 2014). So, although phased array operation still has to be validated, the antenna's small size, high directivity, low cross-coupling, and dominant tangential field component, make the antenna particularly promising for use in such phased-array hyperthermia applicators.

Antenna—MR system interactions were tested on a 1.5 T MRI scanner and found to be negligible in terms of impacting image quality and systems performance. However, since the antennas may be configured for use on higher field MRI systems in the future to obtain a
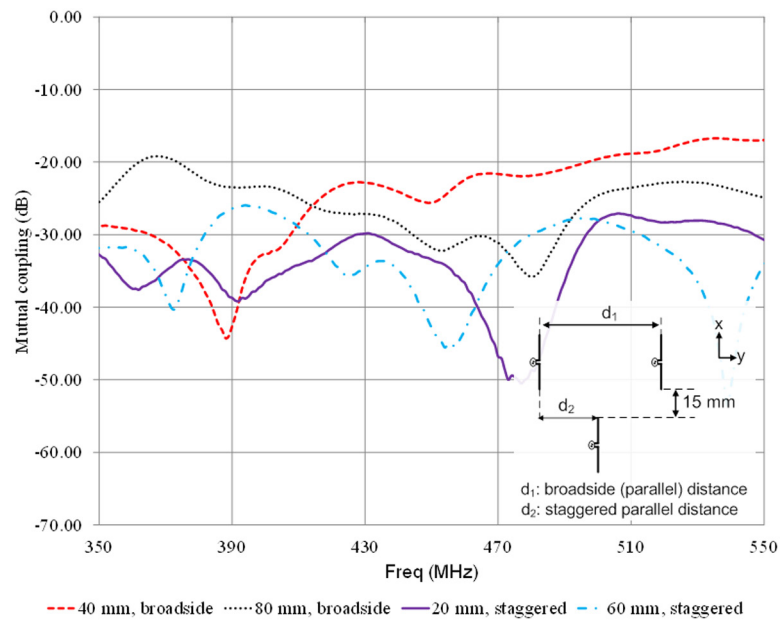
Figure 7. Measured mutual coupling coefficients for the four different arrangements at the nominal water temperature ($T_{\mathrm{DI_{water}}} = 25$ °C). The inlay shows a scheme of the arrangements and dimensions.
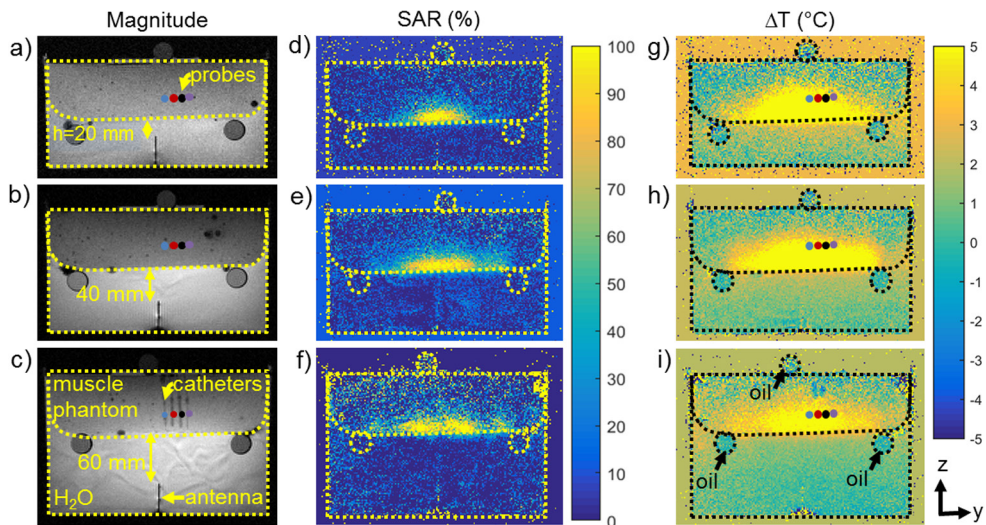
Figure 8. GRE magnitude ((a)–(c)), SAR (1 min, 6 min) ((d)–(f)) and ΔT (1 min, 25 min) ((g)–(i)) distributions measured using for the setup of figure 4 and $h = 2$ cm ((a), (d) and (g)), 4 cm ((b), (e) and (h)) or 6 cm ((c), (f) and (i)). Cross-sections of the cylindrical oil reservoirs, the muscle phantom and the water volume are indicated by dotted lines and the locations of the catheters (grey lines in (c)), reconstructed probes (colored dots) and the very localized distortion by the antenna (black lines in (a)–(c)) are indicated as well. Note that the distortions in de-ionized water (H_2O) region present in the magnitude image are smaller in the ΔT images.
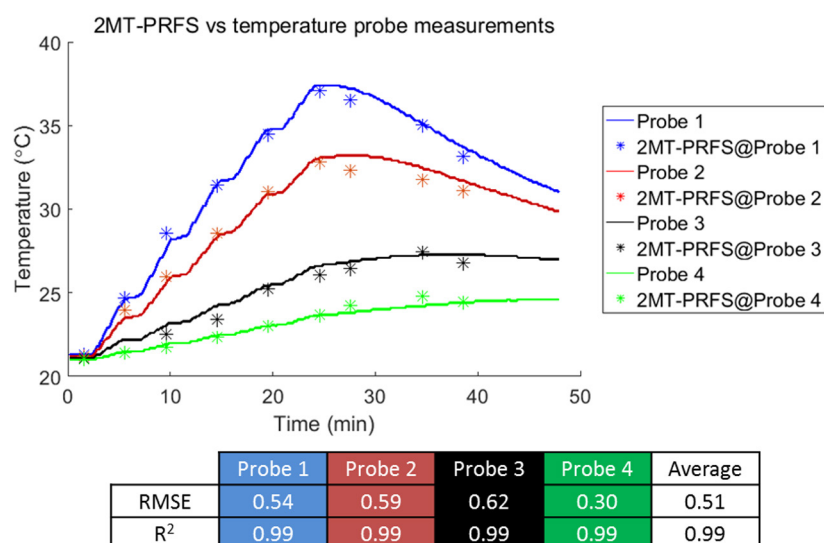
Figure 9. Temporal temperatures measured by probes and the 2MT-PRFS technique for $h = 20$ mm (see figure 8). 2MT-PRFS MRTI results are the average of a 5×5 pixel ROI around the reconstructed probe locations, of which location indications are shown by colored dots in figure 8. Note that MRTI measures temperature increase and that the MRTI temperatures at the start of the experiment were subtracted from the temperature probe measurements.

higher SNR for enabling higher image resolution and/or faster scans, it is advantageous to discuss the potential level of system interaction issues that could be observed at higher $B0$ fields as well. The first question is the printed antenna's interoperability with typical high magnetic field systems, such as those operating at 3.0 T (128 MHz) and 7.0 T (298 MHz), which is well outside of the antenna impedance bandwidth presented in figure 4. Although higher order modes must still be analyzed, in general, reciprocity dictates that a low antenna sensitivity at these frequencies would imply low risks of the antennas radiating spurious $B1+$ fields that may distort the MR scanner's target $B1+$ fields. Distortion of image reception due to coil sensitivity near 433.92 MHz is dependent on the receive coil design, and interaction can be further mitigated by refraining from RF transmission via the antennas and properly terminating the antennas when the scanner is in receive mode. The head and neck area's small cross sectional area mitigates the impact of image shading arising from adverse dielectric effects (Schick 2005). The antenna's impact on systems interactions and image quality at higher B0 fields would then only be a result of material composition and layout, and an extension of effects observed for the 1.5 T case. Since very little impact on image quality was observed at 1.5 T, there is no real reason to believe they will be detrimental at 3.0 T or 7.0 T. However, verification through simulations or experimentation at these field strengths remains necessary.

In contradiction to common practice, we did not apply spatial averaging of MRTI results for generating the SAR distributions. In this way, we could more clearly visualize the increasing impact of noise for the larger phantom-antenna distance. The noise in these images, raises the question if the ESHO quality assurance guidelines, which dictate a heating time of 1 min for SAR assessments (Hand *et al* 1989), are also applicable when using MRTI. Even when applying a heating time of 3 min, we observed considerable noise that, in some cases, exceeded the heating pattern. In this case, the trade-off between sufficient SNR and avoidance of heat conduction for a power-pulse measurement may advocate a shift towards a longer heating time.

Conclusions

A printed Yagi–Uda antenna for a hyperthermia applicator was presented. Using a clinical experimental setup, the performance of this antenna was studied as a single element, in the vicinity of neighbor antennas and in an MR environment. The measured impedance bandwidth of 7.2% is sufficient for the intended application. Simulations show that the dominant *E*-field component is generated in the desired direction (patient axis). Changing the distance between the antenna and the muscle-layer from its nominal value of 40 mm to 20 mm resulted in an acceptable reduction of the impedance bandwidth to 4.9%. The investigation of the effect of temperature showed that only at temperatures exceeding 35 °C the antenna is detuned too much to be used in the applicator. Furthermore, the worst-case measured mutual coupling level was −23 dB at 433.92 MHz, which is well below the specification. In addition, power handling measurements showed a negligible effect of heating up on the antenna characteristics. MR-compatibility was demonstrated by MR imaging of the antenna in the clinical experimental setup. MR imaging showed that the image distortion by the antenna itself is very low and accurate MRTI proved possible. In summary, the performance assessments show that the antenna has high potential for application in a variety of MR-compatible hyperthermia applicators.

Acknowledgments

Conflict of interests

MPS has financial interest in Sensius BV.

References

Adela B, Mestrom R, Paulides M and Smolders A 2013 An MR-compatible Printed Yagi–Uda antenna for a phased array hyperthemia applicator *Proc. of the 7th EuCAP (Gothenburg, Sweden)*
Bakker J F, Paulides M M, Westra A H, Schippers H and Van Rhoon G C 2010 Design and test of a 434 MHz multi-channel amplifier system for targeted hyperthermia applicators *Int. J. Hyperth.* **26** 158–70
Balanis C 2005 *Antenna Theory: Analysis and Design* (New York: Wiley Interscience)
Cheng K S, Stakhursky V, Stauffer P, Dewhirst M and Das S K 2007 Online feedback focusing algorithm for hyperthermia cancer treatment *Int. J. Hyperth.* **23** 539–54
Datta N R, Ordonez S G, Gaipl U S, Paulides M M, Crezee H, Gellermann J, Marder D, Puric E and Bodis S 2015 Local hyperthermia combined with radiotherapy and-/or chemotherapy: recent advances and promises for the future *Cancer Treat. Rev.* **41** 742–53
Fenn A J, Sathiaseelan V, King G A and Stauffer P R 1996 Improved localization of energy deposition in adaptive phased array hyperthermia treatment of cancer *Linc. Lab. J.* **9** 187–96
Franckena M, Canters R, Termorshuizen F, Van Der Zee J and Van Rhoon G 2010 Clinical implementation of hyperthermia treatment planning guided steering: a cross over trial to assess its current contribution to treatment quality *Int. J. Hyperth.* **26** 145–57

Franckena M, Fatehi D, de Bruijne M, Canters R A, van Norden Y, Mens J W, van Rhoon G C and van der Zee J 2009 Hyperthermia dose-effect relationship in 420 patients with cervical cancer treated with combined radiotherapy and hyperthermia *Eur. J. Cancer* **45** 1969–78

Gellermann J, Faehling H, Mielec M, Cho C H, Budach V and Wust P 2008 Image artifacts during MRT hybrid hyperthermia—causes and elimination *Int. J. Hyperth.* **24** 327–35

Gellermann J, Wlodarczyk W, Feussner A, Fahling H, Nadobny J, Hildebrandt B, Felix R and Wust P 2005 Methods and potentials of magnetic resonance imaging for monitoring radiofrequency hyperthermia in a hybrid system *Int. J. Hyperth.* **21** 497–513

Hand J W, Lagendijk J J, Bach Andersen J and Bolomey J C 1989 Quality assurance guidelines for ESHO protocols *Int. J. Hyperth.* **5** 421–8

Henke F M, Joines W T and Samulski T V 2001 Variations of focal regions versus numbers and positions of sources in two-dimensional media *Int. J. Hyperth.* **17** 382–400

Hofstetter L, Yeo D, Dixon W T, Davis C and Foo T K 2011 Fat-referenced MR thermometry using 3-echo phase-based fat water separation method *19th Annual Meeting of the Int. Society for Magnetic Resonance in Medicine (ISMRM) (Montreal, Quebec, Canada)*

Issels R D *et al* 2010 Neo-adjuvant chemotherapy alone or with regional hyperthermia for localised high-risk soft-tissue sarcoma: a randomised phase 3 multicentre study *Lancet Oncol.* **11** 561–70

Issels R D *et al* 2015 13LBA Improved overall survival by adding regional hyperthermia to neo-adjuvant chemotherapy in patients with localized high-risk soft tissue sarcoma (HR-STS): long-term outcomes of the EORTC 62961/ESHO randomized phase III study *18th ECCO—40th ESMO European Cancer Congress (Vienna, Austria)*

Ito K, Furuya K, Okano Y and Hamada L 2001 Development and characteristics of a biological tissue-equivalent phantom for microwaves *Electron. Commun. Japan* I **84** 67–77

Jones E, Thrall D, Dewhirst M W and Vujaskovic Z 2006 Prospective thermal dosimetry: the key to hyperthermia's future *Int. J. Hyperth.* **22** 247–53

Kampinga H H 2006 Cell biological effects of hyperthermia alone or combined with radiation or drugs: a short introduction to newcomers in the field *Int. J. Hyperth.* **22** 191–6

Ludemann L, Wlodarczyk W, Nadobny J, Weihrauch M, Gellermann J and Wust P 2010 Non-invasive magnetic resonance thermography during regional hyperthermia *Int. J. Hyperth.* **26** 273–82

Nadobny J, Fahling H, Hagmann M J, Turner P F, Wlodarczyk W, Gellermann J M, Deuflhard P and Wust P 2002 Experimental and numerical investigation of feed-point parameters in a 3D hyperthermia applicator using different FDTD models of feed networks *IEEE Trans. Biomed. Eng.* **49** 1348–59

Overgaard J 2013 The heat is (still) on—the past and future of hyperthermic radiation oncology *Radiother. Oncol.* **109** 185–7

Paulides M M, Bakker J F, Chavannes N and Van Rhoon G C 2007a A patch antenna design for application in a phased-array head and neck hyperthermia applicator *IEEE Trans. Biomed. Eng.* **54** 2057–63

Paulides M M, Bakker J F, Neufeld E, van der Zee J, Jansen P P, Levendag P C and van Rhoon G C 2007b The HYPERcollar: a novel applicator for hyperthermia in the head and neck *Int. J. Hyperth.* **23** 567–76

Paulides M M, Bakker J F, Hofstetter L W, Numan W C, Pellicer R, Fiveland E W, Tarasek M, Houston G C, van Rhoon G C, Yeo D T and Kotek G 2014 Laboratory prototype for experimental validation of MR-guided radiofrequency head and neck hyperthermia *Phys. Med. Biol.* **59** 2139–54

Paulides M M, Stauffer P R, Neufeld E, Maccarini P F, Kyriakou A, Canters R A, Diederich C J, Bakker J F and Van Rhoon G C 2013 Simulation techniques in hyperthermia treatment planning *Int. J. Hyperth.* **29** 346–57

Paulides M M, Verduijn G M and Van Holthe N 2016 Status quo and directions in deep head and neck hyperthermia *Radiat. Oncol.* **11** 21

Paulides M M, Vossen S H, Zwamborn A P and van Rhoon G C 2005a Theoretical investigation into the feasibility to deposit RF energy centrally in the head-and-neck region *Int. J. Radiat. Oncol. Biol. Phys.* **63** 634–42

Paulides M M, Wielheesen D H, Van der Zee J and Van Rhoon G C 2005b Assessment of the local SAR distortion by major anatomical structures in a cylindrical neck phantom *Int. J. Hyperth.* **21** 125–40

Poot D H and Klein S 2015 Detecting statistically significant differences in quantitative MRI experiments, applied to diffusion tensor imaging *IEEE Trans. Med. Imaging* **34** 1164–76

Rieke V and Butts Pauly K 2008 MR thermometry *J. Magn. Reson. Imaging* **27** 376–90

Rijnen Z, Bakker J F, Canters R A, Togni P, Verduijn G M, Levendag P C, Van Rhoon G C and Paulides M M 2013 Clinical integration of software tool VEDO for adaptive and quantitative application of phased array hyperthermia in the head and neck *Int. J. Hyperth.* **29** 181–93

Rijnen Z, Togni P, Roskam R, van de Geer S G, Goossens R H and Paulides M M 2015 Quality and comfort in head and neck hyperthermia: a redesign according to clinical experience and simulation studies *Int. J. Hyperth.* **31** 823–30

Salim G, Poot D, Numan W, Vogel M, Drizdal T, Paulides M and Klein S 2015 Multipeak multiecho modeling for improved PRF-based thermometry *32nd Annual Scientific Meeting of the ESMRMB (Edinburgh, UK)*

Schick F 2005 Whole-body MRI at high field: technical limits and clinical potential *Eur. Radiol.* **15** 946–59

Stakhursky V L, Arabe O, Cheng K S, Macfall J, Maccarini P, Craciunescu O, Dewhirst M, Stauffer P and Das S K 2009 Real-time MRI-guided hyperthermia treatment using a fast adaptive algorithm *Phys. Med. Biol.* **54** 2131–45

Tarasek M R *et al* 2014 Validation of MR thermometry: method for temperature probe sensor registration accuracy in head and neck phantoms *Int. J. Hyperth.* **30** 142–9

Togni P, Rijnen Z, Numan W C, Verhaart R F, Bakker J F, van Rhoon G C and Paulides M M 2013 Electromagnetic redesign of the HYPERcollar applicator: toward improved deep local head-and-neck hyperthermia *Phys. Med. Biol.* **58** 5997–6009

van der Zee J 2002 Heating the patient: a promising approach? *Ann. Oncol.* **13** 1173–84

van der Zee J, Peer-Valstar J N, Rietveld P J, de Graaf-Strukowska L and van Rhoon G C 1998 Practical limitations of interstitial thermometry during deep hyperthermia *Int. J. Radiat. Oncol. Biol. Phys.* **40** 1205–12

van Rhoon G C 2016 Is CEM43 still a relevant thermal dose parameter for hyperthermia treatment monitoring? *Int. J. Hyperth.* **32** 50–62

van Rhoon G C and Wust P 2005 Introduction: non-invasive thermometry for thermotherapy *Int. J. Hyperth.* **21** 489–95

Winter L, Oberacker E, Paul K, Ji Y, Oezerdem C, Ghadjar P, Thieme A, Budach V, Wust P and Niendorf T 2016 Magnetic resonance thermometry: methodology, pitfalls and practical solutions *Int. J. Hyperth.* **32** 63–75

Winter L, Ozerdem C, Hoffmann W, Santoro D, Muller A, Waiczies H, Seemann R, Graessl A, Wust P and Niendorf T 2013 Design and evaluation of a hybrid radiofrequency applicator for magnetic resonance imaging and RF induced hyperthermia: electromagnetic field simulations up to 14.0 Tesla and proof-of-concept at 7.0 Tesla *PLoS One* **8** e61661

Winter L, Oezerdem C, Hoffmann W, van de Lindt T, Periquito J, Ji Y, Ghadjar P, Budach V, Wust P and Niendorf T 2015 Thermal magnetic resonance: physics considerations and electromagnetic field simulations up to 23.5 Tesla (1GHz) *Radiat. Oncol.* **10** 201

Wust P, Cho C H, Hildebrandt B and Gellermann J 2006 Thermal monitoring: invasive, minimal-invasive and non-invasive approaches *Int. J. Hyperth.* **22** 255–62

Wust P, Fahling H, Wlodarczyk W, Seebass M, Gellermann J, Deuflhard P and Nadobny J 2001 Antenna arrays in the SIGMA-eye applicator: interactions and transforming networks *Med. Phys.* **28** 1793–805

Yeo D, Yang X, Wu J, Hofstetter L W, Piel J E, Fiveland E W, Park K J and Foo T K 2011 Investigation of a dual-function applicator for rf hyperthermia and MRI *19th Annual Meeting of the ISMRM (Montreal, Quebec, Canada)* p 1811